Towards model-based adaptive optics optical coherence tomography

Hans R. G. W. Verstraete,[1,*] Barry Cense,[2] Rolf Bilderbeek,[1] Michel Verhaegen,[1] and Jeroen Kalkman[3]

[1]*Delft Center for Systems and Control, Delft University of Technology, Mekelweg 2, 2628 DC Delft, The Netherlands*

[2]*CORE, Utsunomiya University, Utsunomiya, 320-8540, Japan*

[3]*Department of Imaging Physics, faculty of Applied Sciences, Delft University of Technology, Lorentzweg 1, 2628 DC Delft, The Netherlands*

[*]*h.r.g.w.verstraete@tudelft.nl*

Abstract: The transfer function for optical wavefront aberrations in single-mode fiber based optical coherence tomography is determined. The loss in measured OCT signal due to optical wavefront aberrations is quantified using Fresnel propagation and the calculation of overlap integrals. A distinction is made between a model for a mirror and a scattering medium model. The model predictions are validated with measurements on a mirror and a scattering medium obtained with an adaptive optics optical coherence tomography setup. Furthermore, a one-step defocus correction, based on a single A-scan measurement, is derived from the model and verified. Finally, the pseudo-convex structure of the optical coherence tomography transfer function is validated with the convergence of a hill climbing algorithm. The implications of this model for wavefront sensorless aberration correction are discussed.

OCIS codes: (110.4500) Optical Coherence Tomography; (110.4850) Optical transfer functions; (110.1080) Adaptive optics.

References and links

1. D. Huang, E. Swanson, C. Lin, J. Schuman, W. Stinson, W. Chang, M. Hee, T. Flotte, K. Gregory, C. Puliafito, and J. Fujimoto, "Optical coherence tomography," Science **254**, 1178–1181 (1991).
2. A. Fercher, C. Hitzenberger, G. Kamp, and S. El-Zaiat, "Measurement of intraocular distances by backscattering spectral interferometry," Opt. Commun. **117**, 43 – 48 (1995).
3. B. Cense, N. Nassif, T. Chen, M. Pierce, S.-H. Yun, B. Park, B. Bouma, G. Tearney, and J. de Boer, "Ultrahigh-resolution high-speed retinal imaging using spectral-domain optical coherence tomography," Opt. Express **12**, 2435–2447 (2004).
4. M. Wojtkowski, V. Srinivasan, T. Ko, J. Fujimoto, A. Kowalczyk, and J. Duker, "Ultrahigh-resolution, high-speed, Fourier domain optical coherence tomography and methods for dispersion compensation," Opt. Express **12**, 2404–2422 (2004).
5. R. Leitgeb, C. Hitzenberger, and A. Fercher, "Performance of Fourier domain vs. time domain optical coherence tomography," Opt. Express **11**, 889–894 (2003).
6. B. Povazay, K. Bizheva, A. Unterhuber, B. Hermann, H. Sattmann, A. F. Fercher, W. Drexler, A. Apolonski, W. J. Wadsworth, J. C. Knight, P. S. J. Russell, M. Vetterlein, and E. Scherzer, "Submicrometer axial resolution optical coherence tomography," Opt. Lett. **27**, 1800–1802 (2002).
7. Y. Zhang, J. Rha, R. Jonnal, and D. Miller, "Adaptive optics parallel spectral domain optical coherence tomography for imaging the living retina," Opt. Express **13**(12), 4792-4811 (2005).
8. R. Zawadzki, S. Jones, S. Olivier, M. Zhao, B. Bower, J. Izatt, S. Choi, S. Laut, and J. Werner, "Adaptive-optics optical coherence tomography for high-resolution and high-speed 3D retinal in vivo imaging," Opt. express **13**(21), 8532-8546 (2005).

#226065 - $15.00 USD Received 31 Oct 2014; revised 11 Dec 2014; accepted 11 Dec 2014; published 23 Dec 2014

9. Y. Zhang, B. Cense, J. Rha, R. S. Jonnal, W. Gao, R. J. Zawadzki, J. S. Werner, S. Jones, S. Olivier, and D. T. Miller, "High-speed volumetric imaging of cone photoreceptors with adaptive optics spectral-domain optical coherence tomography," Opt. Express **14**, 4380–4394 (2006).
10. E. J. Fernández, B. Považay, B. Hermann, A. Unterhuber, H. Sattmann, P. M. Prieto, R. Leitgeb, P. Ahnelt, P. Artal, and W. Drexler, "Three-dimensional adaptive optics ultrahigh-resolution optical coherence tomography using a liquid crystal spatial light modulator," Vision research **45**, 3432–3444 (2005).
11. M. Pircher, R. Zawadzki, J. Evans, J. Werner, and C. Hitzenberger, "Simultaneous imaging of human cone mosaic with adaptive optics enhanced scanning laser ophthalmoscopy and high-speed transversal scanning optical coherence tomography," Opt. Lett. **33**, 22–24 (2008).
12. S. Bonora and R. J. Zawadzki, "Wavefront sensorless modal deformable mirror correction in adaptive optics: optical coherence tomography," Opt. Lett. **38**, 4801–4804 (2013).
13. Y. Jian, J. Xu, M. A. Gradowski, S. Bonora, R. J. Zawadzki, and M. V. Sarunic, "Wavefront sensorless adaptive optics optical coherence tomography for in vivo retinal imaging in mice," Biomed. Opt. Express **5**, 547–559 (2014).
14. M.-R. Nasiri-Avanaki, S. Hojjatoleslami, H. Paun, S. Tuohy, A. Meadway, G. Dobre, and A. Podoleanu, "Optical coherence tomography system optimization using simulated annealing algorithm," in *Proceedings of Mathematical Methods and Applied Computing*, (WSEAS, 2009), pp. 669–674.
15. J. Antonello, M. Verhaegen, R. Fraanje, T. van Werkhoven, H. C. Gerritsen, and C. U. Keller, "Semidefinite programming for model-based sensorless adaptive optics," J. Opt. Soc. Am. A **29**, 2428–2438 (2012).
16. M. Booth, "Wave front sensor-less adaptive optics: a model-based approach using sphere packings," Opt. Express **14**, 1339–1352 (2006).
17. S. G. Adie, B. W. Graf, A. Ahmad, P. S Carney, and S. A. Boppart, "Computational adaptive optics for broadband optical interferometric tomography of biological tissue," PNAS **109**(19), 7175-7180 (2012).
18. J. A. Izatt, M. D. Kulkarni, H.-W. Wang, K. Kobayashi, and M. V. Sivak Jr, "Optical coherence tomography and microscopy in gastrointestinal tissues," IEEE J. Sel. Topics Quantum Electron. **2**, 1017–1028 (1996).
19. J. M. Schmitt, A. Knuttel, M. Yadlowsky, and M. Eckhaus, "Optical-coherence tomography of a dense tissue: statistics of attenuation and backscattering," Phys. Med. Biol. **39**, 1705 (1994).
20. J. A. Izatt, E. A. Swanson, J. G. Fujimoto, M. R. Hee, and G. M. Owen, "Optical coherence microscopy in scattering media," Opt. Lett. **19**, 590–592 (1994).
21. T. G. Van Leeuwen, D. Faber, and M. Aalders, "Measurement of the axial point spread function in scattering media using single-mode fiber-based optical coherence tomography," IEEE J. Sel. Topics Quantum Electron. **9**, 227–233 (2003).
22. G. Hausler and M. W. Lindner, ""Coherence radar" and "spectral radar" new tools for dermatological diagnosis," J. Biomed. Opt. **3**, 21–31 (1998).
23. J. Y. Wang and D. E. Silva, "Wave-front interpretation with Zernike polynomials," Appl. Opt. **19**, 1510–1518 (1980).
24. J. Goodman, *Introduction to Fourier Optics* (McGraw-Hill, 2008).
25. M. Gu, C. Sheppard, and X. Gan, "Image formation in a fiber-optical confocal scanning microscope," J. Opt. Soc. Am. A **8**, 1755–1761 (1991).
26. D. G. Voelz, *Computational Fourier Optics: a MATLAB Tutorial* (SPIE, 2011).
27. L. N. Thibos, R. A. Applegate, J. T. Schwiegerling, and R. Webb, "Standards for reporting the optical aberrations of eyes," J. Refract. Surg. (18)5, S652-S660 (2002).
28. G.-M. Dai, "Modified Hartmann–Shack wavefront sensing and iterative wavefront reconstruction," Proc. SPIE **2201**, 562–573 (1994).
29. H. Verstraete, M. Verhaegen, and J. Kalkman, "Modeling the effect of wave-front aberrations in fiber-based scanning optical microscopy," in *Imaging and Applied Optics,* (Optical Society of America, 2013), paper JTu4A.13.
30. J. R. Fienup and J. J. Miller, "Aberration correction by maximizing generalized sharpness metrics," J. Opt. Soc. Am. A **20**, 609–620 (2003).
31. D. Débarre, E. J. Botcherby, T. Watanabe, S. Srinivas, M. J. Booth, and T. Wilson, "Image-based adaptive optics for two-photon microscopy," Opt. Lett. **34**, 2495–2497 (2009).
32. S. A. Rahman and M. J. Booth, "Adaptive optics for high-resolution microscopy: wave front sensing using back scattered light," in "SPIE MOEMS-MEMS," (International Society for Optics and Photonics, 2012), 82530I.
33. L. N. Thibos, X. Hong, A. Bradley, and X. Cheng, "Statistical variation of aberration structure and image quality in a normal population of healthy eyes," J. Opt. Soc. Am. A **19**, 2329–2348 (2002).

1. Introduction

Optical coherence tomography (OCT) is a technique for non-invasive, *in vivo* imaging of tissue [1, 2]. Its main application is found in opthalmology, where it is used for the 3D imaging of the cornea and retina [3–5]. The axial resolution of OCT is obtained through low coherence interferometry and is inversely proportional to the source bandwidth. Using ultra-broadband

#226065 - $15.00 USD Received 31 Oct 2014; revised 11 Dec 2014; accepted 11 Dec 2014; published 23 Dec 2014

sources, axial resolutions below 1 μm have been recorded [6]. The lateral resolution of OCT is determined by conventional optical lens focusing. Hence, the lateral resolution improves by using a larger pupil. In OCT imaging of the retina the lateral resolution is hampered by the small pupil size ($<$ 2 mm). Moreover, when the pupil size is increased, large ocular aberrations are introduced. It has been demonstrated that high lateral resolutions can be obtained by using adaptive optics (AO) to correct the optical wavefront aberrations on large pupils ($>$2 mm). Combining the high axial resolution of OCT with the high lateral resolution of AO results in ultra-high resolution AO-OCT imaging in three dimensions. Such systems have been reported in [7–10] and demonstrated lateral and axial resolution up to 3 μm and 2- 3 μm, respectively. As a result, AO-OCT has made it possible to image the 3D architecture of individual rods and cones *in vivo* in the human eye [9, 11].

Current AO-OCT setups usually rely on wavefront sensors such as the Shack-Hartmann wavefront sensor. In general, wavefront sensors have several drawbacks. First, a loss of signal to noise ratio in the OCT signal occurs because light from the object is directed away from the sensor (if no alternative imaging device is used as a wavefront sensor). Second, specular reflection of optical components or from the eye prevent the wavefront sensor from giving an accurate estimation of the aberrations. Third, the magnitude and accuracy of the measured wavefront aberrations are limited by the wavefront sensor design. Due to the large aberrations present in the human eye, a trade-off is usually made between the maximum aberration that can be measured and the accuracy of the wavefront estimation. Fourth, since wavefront sensors are located outside the imaging path, non common-path errors with the imaged signal occur. In other words different aberrations are estimated by the SH wavefront sensor than are present in the optical path for the OCT image. Finally, the cost of the wavefront sensor increases the overall cost of any adaptive optics system. This increased cost hampers commercial and medical use of AO-OCT devices. Several authors have successfully applied wavefront sensorless (WFS) AO algorithms to OCT [12–14] to mitigate these disadvantages. WFS approaches are based on phenomenological image quality metrics that are optimized to achieve aberration free images. If analytical expressions for the transfer function of the OCT signal for different aberrations are known, more efficient metrics and algorithms can be found and the region of convergence can be determined. For example, in [15, 16] it is shown that the use of models can improve the convergence speed of WFS algorithms. In [17] a general model is used, based on a synthetic aperture and Zernike modal decomposition, for a software based image optimization. The optimization is based on a sharpness and intensity metric.

Until now, only single aberrations have been modeled for OCT. The tip/tilt aberrations are modeled in the context of galvanometric mirrors, that are used for scanning across the sample. The defocus aberration is studied in the context of the axial transfer function for single-mode fiber (SMF) based OCT systems. Studies [18–21] showed that the amount of backscattered signals, which is due to optical properties of the tissue, is also influenced by the optical components of the OCT setup. A simplified axial transfer function is proposed in [21] based on the overlap of the Gaussian beam profile arising from the SMF. The proposed axial transfer function assumes the propagation of a perfect Gaussian beam profile without lateral optical wavefront aberrations other than a fixed defocus introduced by the lens. This transfer function is used to correct for OCT system properties in the backscattered measured signal to determine the attenuation coefficient of tissue from OCT scans. In general, OCT transfer function models distinguish between a specular reflector and a backscattered sample. In the axial defocus model in [21] the interaction of a Gaussian beam with the scattering medium is modeled by removing the defocus curvature of the Gaussian beam at the sample.

The goal of this paper is to model and validate the effect of arbitrary optical wavefront aberrations on the OCT signal for mirror and scattering media reflectors. This model is used to

#226065 - $15.00 USD Received 31 Oct 2014; revised 11 Dec 2014; accepted 11 Dec 2014; published 23 Dec 2014

correct for defocus and predict the convergence of a WFS algorithm.

2. OCT model

OCT is based on a combination of confocal and coherent gating [22]. Confocal gating is implemented by single mode fibers that act as pinholes for outgoing and returned light. Coherence gating is based on low coherence, i.e. large optical bandwidth interference, to detect only a thin section of the sample. The confocal and coherent detection of the OCT system all take place in the OCT sample arm, which can be modeled as in Fig. 1. A first lens (CL), conjugated to the

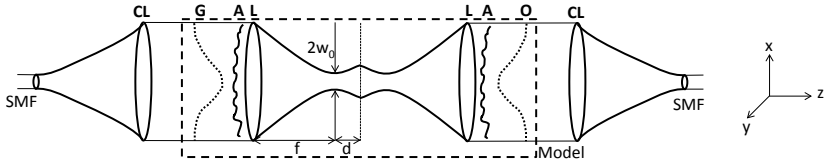

Fig. 1. Geometry model for SMF-OCT. A collimator lens (CL) collimates the beam to a planar wavefront with Gaussian distribution (G). The sample lens (L) with aberrations (A) focuses the light on the sample at distance $f+d$. Light is reflected/scattered by the sample, shown here in transmission. The overlap integral (O) with the Gaussian mode is calculated to quantify the coupling efficiency into the SMF.

sample lens, is used to collimate the beam. A second lens (L), the sample lens, which contains aberrations (A), is used to focus the light on the sample located a distance d from the actual focus f of the sample lens. Light reflected from a thin slice of the sample goes through the same path back to the SMF, which is shown in this model as transmission. The sample can be a mirror or a thin slice of tissue, which we model here separately.

2.1. OCT mirror model

After collimation by the collimator lens the optical field emitted from the single mode fiber has a Gaussian distribution with a flat wavefront. This planar Gaussian wavefront (G) is described by

$$G(x,y) = C\exp\left(-\frac{1}{w^2}(x^2+y^2)\right). \tag{1}$$

Here, C is the amplitude, and w is the beam waist of the collimated fundamental Gaussian fiber mode. Next, the wavefront traverses optical aberrations. The aberrations (A) in the pupil plane are denoted as

$$A(x,y,\alpha) = \exp\left(ikW(x,y)\right). \tag{2}$$

Here, k is the wave number $\frac{2\pi}{\lambda}$, i is the imaginary number $\sqrt{-1}$. Normalized Zernike polynomials are used over a circular pupil [23] to represent $W(x,y) = \alpha^T Z(x,y)$, the vector α contains the corresponding Zernike coefficients, $Z(x,y)$ is a vector of the corresponding Zernike polynomials.

The aberrated optical wavefront is focused by a lens. The paraxial approximation of the focusing sample lens (L) with a circular pupil is given by

$$L(x,y) = \exp(-ikf)\exp\left(\frac{-ik}{2f}(x^2+y^2)\right)\mathrm{circ}\left(\frac{\sqrt{x^2+y^2}}{r_{pupil}}\right). \tag{3}$$

For the lens the Fresnel approximation is used with focal length f. Following Goodman [24], the circular pupil function $\mathrm{circ}(\sqrt{x^2+y^2}/r_{pupil})$ is a circle with radius r_{pupil}. Values inside

#226065 - $15.00 USD Received 31 Oct 2014; revised 11 Dec 2014; accepted 11 Dec 2014; published 23 Dec 2014

the circle are set to 1, outside the circle to 0, and on the border to 0.5. The pupil function is determined by the smallest pupil in the optical setup, in our case the deformable mirror, which limits the beam radius to $r_{pupil} = 3.61$ mm.

Fresnel diffraction (F) [24] approximates the propagation of an arbitrary wavefront $U(x_1, y_1)$ to the plane (x_2, y_2) over an OPL z as,

$$U_z(x_2, y_2) = F(U(x_1, y_1), z) = \frac{\exp(ikz)}{i\lambda z} \iint U(x_1, y_1) \exp\left(\frac{ik}{2z}\left[(x_2 - x_1)^2 + (y_2 - y_1)^2\right]\right) \mathrm{d}x_1 \, \mathrm{d}y_1. \tag{4}$$

In the mirror model the Gaussian distributed wavefront (G) passes through aberrations (A) and the sample lens (L) and propagates (Fresnel diffraction) over a distance $f + d$ to reflect on the mirror and then propagates backwards over the distance $f + d$. We describe the latter by a Fresnel propagation over $2(f + d)$. Hence, the wavefront right before the sample lens (L) is

$$U_1(x_3, y_3, d, \alpha) = F\left[G(x_1, y_1) L(x_1, y_1) A(x_1, y_1, \alpha), 2(f + d)\right]. \tag{5}$$

Again, wavefront U_1 traverses the sample lens (L) with aberrations (A). Finally, an overlap integral (O) of the field with the Gaussian mode of the collimated beam is taken. Since the SMF only accepts a Gaussian wavefront identical to the collimated Gaussian mode, we take the overlap integral of the reflected light with this Gaussian wavefront to determine the total field coupled back into the fiber from the sample. The overlap integral [25] for an arbitrary wavefront $U(x, y)$ with the Gaussian mode $G(x, y)$ is defined as

$$O(U(x, y)) = \frac{\iint_{-\infty}^{\infty} U(x, y) G^*(x, y) \, \mathrm{d}x \, \mathrm{d}y}{\iint_{-\infty}^{\infty} |G(x, y)|^2 \, \mathrm{d}x \, \mathrm{d}y}. \tag{6}$$

The total intensity coupled back into the SMF is then denoted by

$$h_1(d, \alpha) = \left|O\left[U_1(x_3, y_3, d, \alpha) L(x_3, y_3) A(x_3, y_3, \alpha)\right]\right|^2. \tag{7}$$

2.2. Scattering medium OCT model

The scattering medium transfer function is very similar to the mirror transfer function. The only difference is the interaction with the scattering medium. The Gaussian beam (G) traverses the sample lens (L) with aberrations (A) and interacts with the sample after propagating an OPL $f + d$. In the scattering medium we assume that the lateral phase relation of the wavefront is lost and a new plane wave is formed with a perfect planar wavefront. This is modeled by taking the modulus of the field, $|U(x, y)|$, at the position of the sample, which reduces the original phase of the wavefront laterally to a constant phase. The wavefront U_2 represents the wavefront after having interacted with the sample.

$$U_2(x_2, y_2, d, \alpha) = \left|F\left[G(x_1, y_1) L(x_1, y_1) A(x_1, y_1, \alpha), f + d\right]\right| \tag{8}$$

The wavefront U_2 propagates an OPL of $f + d$ to the aberrated sample lens, which is represented by the wavefront U_3,

$$U_3(x_3, y_3, d, \alpha) = F\left[U_2(x_2, y_2, d, \alpha), f + d\right]. \tag{9}$$

Wavefront U_3 again traverses the sample lens (L) with aberrations (A) and the intensity coupled into the fiber is determined with the overlap integral (O). The total intensity coupled into the SMF fiber is

$$h_2(d, \alpha) = \left|O\left[U_3(x_3, y_3, d, \alpha) L(x, y) A(x, y, \alpha)\right]\right|^2. \tag{10}$$

#226065 - $15.00 USD Received 31 Oct 2014; revised 11 Dec 2014; accepted 11 Dec 2014; published 23 Dec 2014

The functions $h_1(d,\alpha)$ and $h_2(d,\alpha)$ are called OCT transfer functions for the mirror and scattering medium, respectively. These equations represent the intensity that is coupled back into the fiber. It is important to note that the OCT signal, defined as the magnitude of the Fourier transform, scales with the sample arm field and thus with $\sqrt{h_1}$ and $\sqrt{h_2}$. The results for the transfer functions are numerically calculated in MATLAB using the numerical Fresnel propagation code in [26].

2.3. Single step defocus correction

If the AO-OCT setup and sample lens are well-known and calibrated, then a single step correction for the defocus can be implemented. The change in focal length d is related to the Zernike defocus coefficient α_4 and the original focal length f as follows,

$$-\frac{1}{2(f+d)}(x^2+y^2) = -\frac{1}{2f}(x^2+y^2) + 2\sqrt{3}\alpha_4\frac{(x^2+y^2)}{r_{pupil}^2}. \tag{11}$$

In Eq. (11) the left hand side is the quadratic phase factor for the lens focused at a distance $f+d$ and the second term on the right hand side is the Zernike defocus. As a result, the defocus Zernike coefficient is derived as

$$\alpha_4 = \frac{r_{pupil}^2}{4\sqrt{3}}\left(\frac{1}{f}-\frac{1}{f+d}\right). \tag{12}$$

In the equations above r_{pupil} is the radius of the pupil, defined by the smallest pupil in the setup (the deformable mirror), on which the Zernikes are defined. The index proposed by Thibos et al. [27] is used to order the Zernike coefficients α (4 corresponds to the defocus). Equation (12) allows to directly calculate the defocus coefficient α_4 from the distance d the sample is out of focus.

3. Materials and methods

AO-OCT measurements are performed on an adaptive optics OCT system based on single mode fibers and a Michelson interferometer, shown in Fig. 2. The light source is a fiber coupled super luminescent diode (Superlum Broadlighter D-840-HP-I) with a bandwidth of 100 nm and a center wavelength of 840 nm. The fiber from the source is a single mode fiber with a 4 μm core diameter coupled to a fiber coupler (Gould Fiber Optics Corning HI-780) with a splitting ratio of 50/50. Light is detected with a spectrometer (Wasatch Photonics Cobra UHR) with 4096 pixels that cover a wavelength range from 650 nm to 950 nm. The integration time and line-time are set to 23 μs and 25 μs, respectively.

The two arms from the fiber-based interferometer both have 3-paddle polarization controllers (Thorlabs FPC560) and light exiting the sample and reference arm fibers is collimated by a fiber collimator lens (Thorlabs AC254-030-B). The reference arm consists of a folded, collimated beam covering a distance of 3.8 m. In both sample and reference arm a collimated Gaussian beam with a 3.4 mm beam waist $\left(e^{-2}\right)$ starts from the fiber collimator lens. The sample arm consists of pairs of parabolic mirrors that are used to conjugate the planes of the fiber collimator, deformable mirror (DM) and sample lens. The parabolic mirrors PM1 (Edmund Optics 50.8 $\times$ 304.8 mm PFL 15) and PM2 (Edmund Optics 50.8 $\times$ 635.0 mm PFL 15) in Fig. 2 are off-axis parabolic gold mirrors that (de)magnify the beam 2.08 times. The deformable mirror (Imagine Eyes Mirao52) has 52 actuators and a stroke of 50 μm. At the end of the reference and sample arm the sample lens with a focal length of 45 mm (Thorlabs AC254-045-B) focuses the light on a mirror (Thorlabs KM100-E03) and the sample, respectively. An OKOtech Shack-Hartmann (SH) wavefront sensor, 1-inch optical format, with a lenslet array pitch of 300 μm and focal

#226065 - $15.00 USD Received 31 Oct 2014; revised 11 Dec 2014; accepted 11 Dec 2014; published 23 Dec 2014

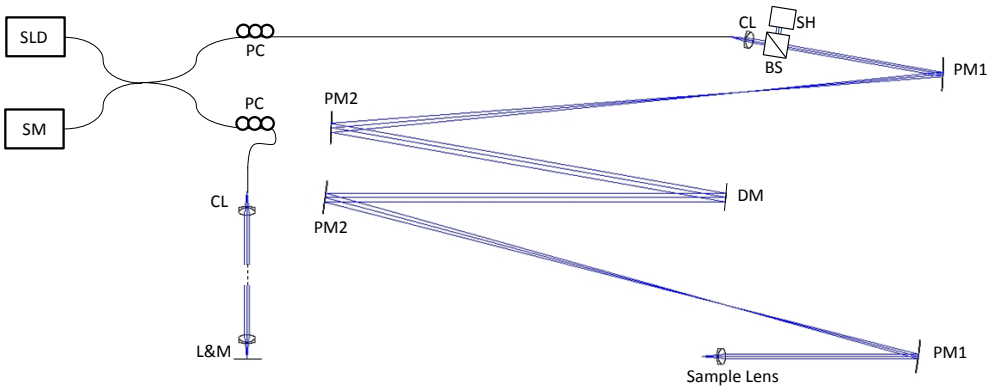

Fig. 2. Schematic overview of the AO-OCT Setup. SMF fibers are indicated by a single line. The free space light is indicated by three lines. SLD = super luminescent diode. SM = spectrometer. PC = polarization controllers. CL = fiber collimator lens. L&M are the lens and mirror for the reference arm. SH = Shack-Hartmann wavefront sensor. BS = beam-splitter. PM1 and PM2 are parabolic mirrors. DM = deformable mirror.

length 18.6 mm, is placed perpendicular to the optical beam path. A pellicle beam splitter (Thorlabs BP108) directs 8% of the light towards the SH and 92% to the fiber. The SH pupil is conjugated to the pupil plane. The SH mask to CCD distance is 16.56 mm.

From the SH images the modal wavefront is reconstructed using the method described in [28]. The diameter of the DM is the smallest pupil and acts as a field stop that determines the maximum pupil size. The DM diameter is 15 mm and after conjugation through the parabolic mirrors the pupil radius is $r_{pupil} = 3.61$ mm. This pupil radius, r_{pupil}, is used for the wavefront reconstruction in the SH sensor as well as in the circular pupil function for the model.

The acquired spectra are processed into OCT A-scans in the following way. First, the spectrum of the reference arm is subtracted. Second, since the pixels of the spectrometer correspond to a non-equidistant k axis, the data is linearly interpolated in k based on a calibration table provided by the manufacturer. After interpolation the fast Fourier transform (FFT) is taken over the spectrum. The magnitude of the FFT is used as the OCT-signal.

The measured axial resolution is 3.9 μm (FWHM), which is in good agreement with the coherence length of the Superlum source spectrum, which is 3.5 μm (FWHM). The sensitivity is determined to be -94 dB by measuring the signal to noise ratio between peak signal and the RMS noise.

Odd and even Zernike aberrations are set on the DM, such that perfect Zernike aberrations are displayed in the conjugate plane of the sample lens. Normalized Zernike aberrations with index 1 to 9 are applied to the DM (tip, tilt, defocus, 2 astigmatisms, 2 comas and 2 trefoils). The tip and tilt are left out for the scattering medium, because these aberrations correspond to lateral scanning over the sample, which is performed by a translation stage. The aberration coefficients are varied between -0.45 μm to 0.45 μm.

For the mirror measurements 512 A-scans are taken at the same lateral position. All of the OCT signal in the A-scans is then averaged over time and all depth to a scalar and normalized (divided by the maximum value in a set of measurements). This scalar represents the OCT signal for the mirror measurements.

For the scattering medium measurement, 512 A-scans are taken of a sample consisting of 4 layers of Scotch tape attached on a translation stage. These 512 A-scans are averaged over time and out of the averaged A-scan four depth points at zero aberrations are taken. Several differ-

#226065 - $15.00 USD Received 31 Oct 2014; revised 11 Dec 2014; accepted 11 Dec 2014; published 23 Dec 2014

ent aberrations are applied to the DM and the same four depth points are scaled by the same normalization factor. These four points represent the OCT signal for the scattering medium measurements.

4. Results

Figure 3 shows the OCT measurements on a mirror for varying aberrations applied on the DM. The measurements are plotted together with numerical results obtained for the mirror model. The mirror model is in good agreement with the measurements, especially for small aberrations. The model predicts almost no loss in OCT signal for the odd aberrations (index 1-2, 6-9), because these aberrations are canceled due to the double pass through the optical system. The higher order odd aberrations (comas and trefoils) show a loss of OCT signal stronger than the results predicted by the model. We attribute this to slight misalignments, which cause an imperfect cancellation of the odd aberrations leading to the introduction of other aberrations in the wavefront.

Figure 4 shows the measured Zernike coefficients on the SH sensor, for modes with index 1 to 20, obtained from the SH wavefront sensor. For even aberrations applied on the DM (index 3 to 5) the measured wavefront aberrations on the SH are about twice as large as those that have been put on the DM, i.e. the slope of the measurements on the SH sensor for even aberrations in Fig. 4 is about 2. The Zernike coefficients of the SH sensor show that for odd aberrations (index 1 to 2 and 6 to 9) the wavefront aberration cancels in the SH measurement. However, other aberrations appear (mostly tip, tilt, and defocus) due to imperfect cancellation of the odd aberrations.

Figure 5 shows OCT measurements on the scattering medium versus the applied aberration for index 3 to 9. The OCT measurements have a greater standard deviation than the mirror measurements due to movement of the sample and the much lower signal strength. The measurements are compared to the scattering medium model and show good agreement to the scattering medium model. It can be observed that the obtained functions for the scattering medium for astigmatisms and defocus are broader than the corresponding functions for the mirror measurements. The FWHM for the defocus curve of the mirror model is approximately 0.2 μm, while the FWHM for the defocus curve of the scattering medium model is approximately 0.4 μm. Moreover, the transfer functions have a global maximum at zero aberrations for the given aberrations from -0.45 to 0.45 μm. In comparison to the mirror model a clear maximum is visible for both odd and even applied aberrations.

The corresponding Zernike coefficients, index 1 to 20, measured on the SH wavefront sensor are shown in Fig. 6. The SH sensor measurement gives aberrations similar to the aberration applied to the DM, even though the optical path passes the DM twice. This means that light is not specularly reflected, but diffuse and that the phase of the wavefront is lost after interaction with the scattering medium.

Based on the validity of our wavefront model we apply the model for one step defocus correction, as shown in Fig. 7. For this experiment the sample is moved a fixed distance out of focus (0.39 mm in Fig. 7). The optical path length moved out of focus, d, is determined by the displacement of the target depth of the sample on the OCT A-scan measurement and used to calculate α_4 based on Eq. (12). Other parameters used in this equation are the pupil radius r_{pupil} = 3.61 mm, and the focal length of the sample lens f = 45 mm. The theoretical prediction of Eq. (12) for all displacements is shown in Fig. 7(c) as the black line. The red dots correspond to the Zernike defocus coefficient, α_4, that maximized the OCT signal at that depth in the A-scan. Figure 7 shows the sample before Fig. 7(a) and after Fig. 7(b) defocus correction, both are displayed with the same intensity scale. Clearly, the sample in focus has a higher OCT signal.

Finally, we demonstrate that the model gives us insight into sensorless wavefront correction.

#226065 - $15.00 USD Received 31 Oct 2014; revised 11 Dec 2014; accepted 11 Dec 2014; published 23 Dec 2014

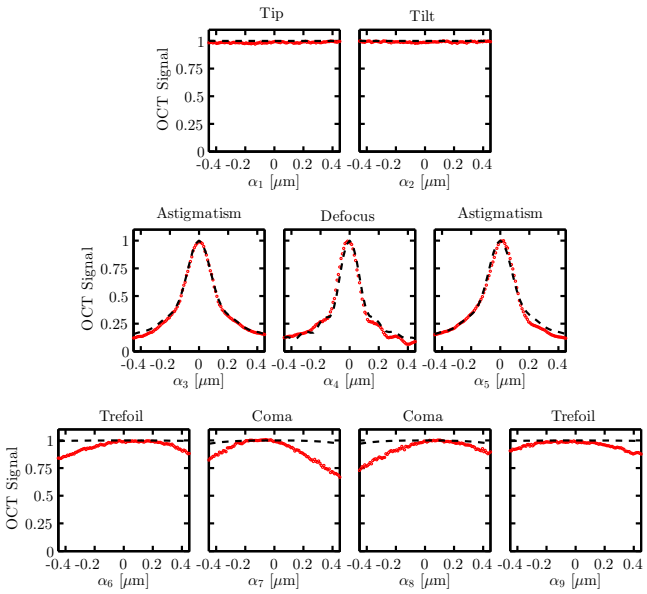

Fig. 3. OCT signal measurements on a mirror versus applied aberration for index 1-9. Measurements (red markers) and numerical results (dashed black line) of the transfer function $\sqrt{h_1(0,\alpha)}$ for the OCT signal are shown. The standard deviation of the measurements is smaller than the marker size.

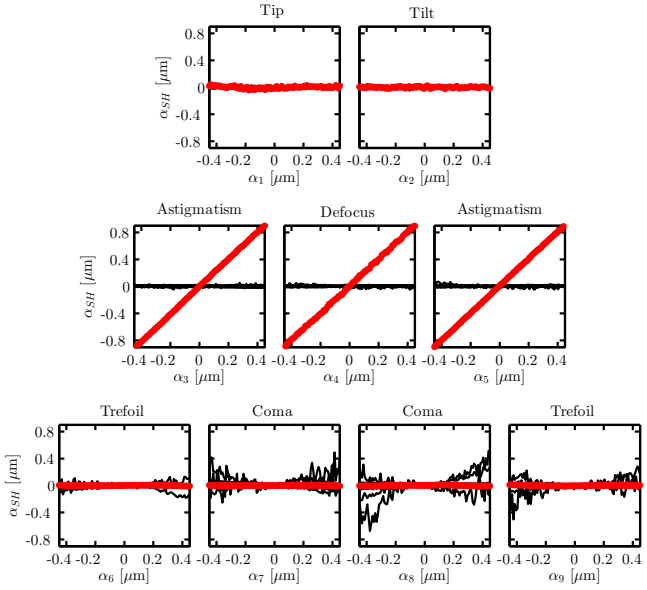

Fig. 4. Shack-Hartmann wavefront measurements on a mirror versus applied wavefront aberration, for index 1-9. Measured wavefront aberrations are index 1-20. The measured aberration that is identical to the applied aberration is in red, all other aberrations are indicated in black.

We test a sequential optimization algorithm similar to [12] for aberrations with RMS error smaller than 0.4 μm. The applied aberrations are limited to the Zernike modes with index 3 to

#226065 - $15.00 USD Received 31 Oct 2014; revised 11 Dec 2014; accepted 11 Dec 2014; published 23 Dec 2014

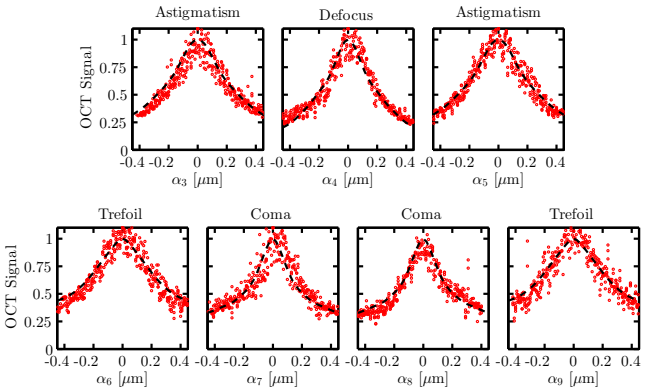

Fig. 5. OCT signal measurements on a scattering medium versus applied aberration for index 3-9. Measurements (red markers) and numerical results (dashed black line) of the transfer function $\sqrt{h_2(0,\alpha)}$ for the OCT signal are shown.

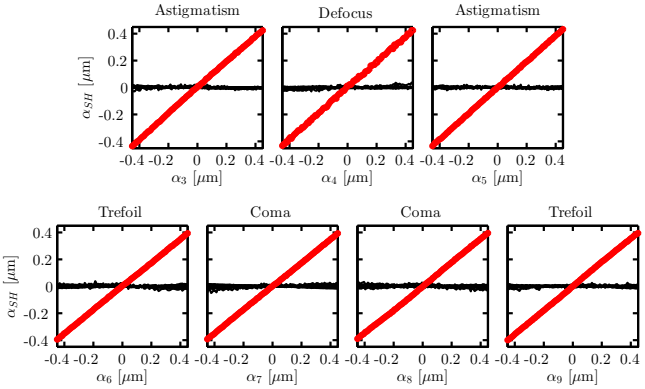

Fig. 6. Shack-Hartmann wavefront measurements on a scattering medium versus applied wavefront aberration, for index 3-9. Measured wavefront aberrations are index 1-20. The measured aberration that is identical to the applied aberration is in red, all other aberrations are indicated in black.

9 (similar to Fig. 5). The results for this test are shown in Fig. 8. Figure 8(a) shows a single optimization for a random aberration applied to the DM. It shows the magnitude of the merit function (OCT signal) while the algorithm scans through Zernike modes with index 3 to 9 for the first time and adds the argument corresponding to the maximum for each mode to the DM to correct this aberration. In Fig. 8(b) the value of the merit function is shown after the algorithm has converged for 100 different starting aberrations, all with RMS error smaller than 0.4 μm. The test shows that the sequential optimization algorithm converges to the same magnitude for 100 different initial aberrations all with an RMS wavefront error smaller than 0.4 μm. On average it takes 20 seconds for the algorithm to converge.

#226065 - $15.00 USD Received 31 Oct 2014; revised 11 Dec 2014; accepted 11 Dec 2014; published 23 Dec 2014

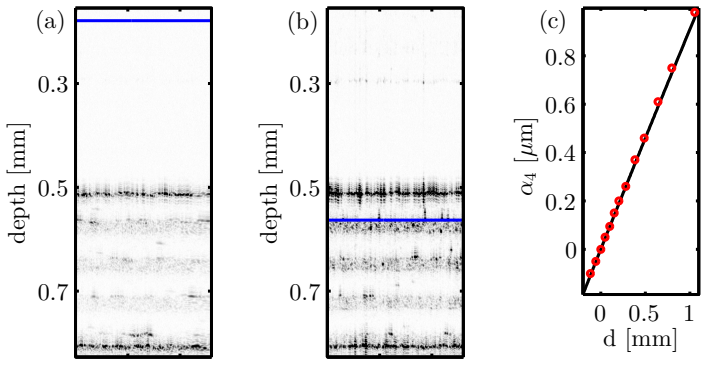

Fig. 7. OCT B-scans of the tissue phantom. (a) Out of focus. (b) After single shot focus correction. Blue lines indicate the location of the focal plane. (c) Results of the one shot defocus correction. Zernike coefficients are determined from Eq. (7) (solid black line) and from measurements (red circles).

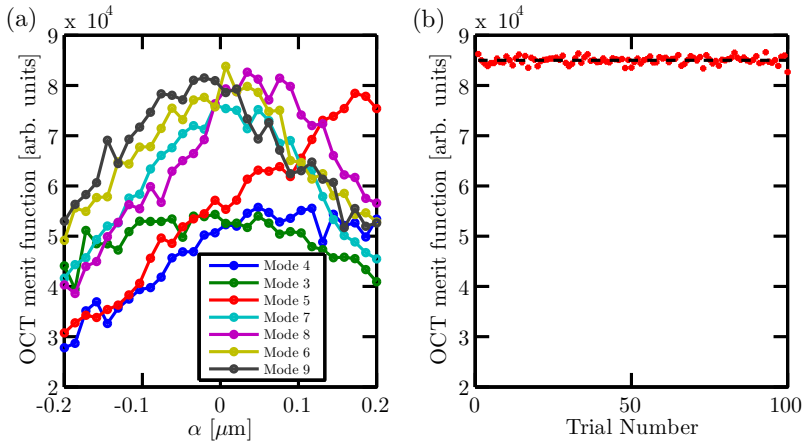

Fig. 8. (a) Merit function (value of OCT signal) during a single step in the sequential optimization process. Only the first search iteration of every Zernike mode is shown for index 3-9. Further iterations resulted in an increased value of the merit function. (b) Optimized merit function after complete optimization process for 100 random aberrations with RMS wavefront error <0.4 μm. For all 100 aberrations the maximum OCT signal is found.

5. Discussion

The transfer functions for the OCT signal for mirror and scattering medium in Eq. (7) and Eq. (10) are calculated based only on experimental parameters. Both transfer functions match the experimental results well, as shown in Fig. 3 and 5.

The Shack-Hartmann measurements show a large difference between the wavefront returning from the mirror and the scattering medium. The phase aberrations of the reflected wavefront are doubled for even aberrations and are canceled for odd aberrations for measurements on the mirror. The specular reflection of the mirror causes the odd aberrations to cancel and the even aberrations to double. Hence, these aberrations are difficult to detect from a decrease in the OCT signal of a specular reflector. Even though the OCT signal for the mirror measurements does not decrease a lot for the odd aberrations (index 1-2 and 6-9) in Fig. 3, our calculations show that

#226065 - $15.00 USD Received 31 Oct 2014; revised 11 Dec 2014; accepted 11 Dec 2014; published 23 Dec 2014

the lateral resolution (quantified by the FWHM of the focal spot on the sample) decreases for an increasing magnitude of the odd aberrations [29]. Hence, image quality metrics should not only be based on intensity but also on sharpness when dealing with specular reflecting objects, which might also occur in OCT. This has been proposed on an ad-hoc basis [30,31], but clearly follows from our analysis.

Our model and measurements show that the lateral phase relations are lost when the wavefront interacts with the scattering sample as the Shack-Hartmann measures the same size of aberration as applied to the DM. The axial defocus model of van Leeuwen et al. [21] for a scattering medium is also based on removal of defocus wavefront curvature of the Gaussian beam after it interacted with the scattering medium. This supports the use of our phase reset operator in the scattering medium model, which is based on the same principle. Others have reported partial loss of wavefront phase upon reflection from a scattering medium [32]. This may be attributed to the presence of both specular and diffuse reflection components in their measurement.

To further validate the proposed OCT transfer functions, they are compared with the well established Lorentzian axial transfer functions from [21]. The numerical results of the OCT signal transfer functions $h_1(d,0)$ and $h_2(d,0)$ for an axial displacement of the sample, d, for the mirror and scattering medium are similar to the two different Lorentzian functions proposed in [21] when the pupil is large enough compared to the Gaussian waist of the beam. For large pupils, $h_1(d,0)$ and $h_2(d,0)$ correspond to the Lorentzian functions, similar to the analytical expression in [21, 29]. The developed transfer functions can be used to correct OCT A-scans for system properties including all aberrations. Hence, potentially improving the estimation of tissue attenuation coefficients from OCT data in the presence of other aberrations besides defocus.

These models can be related to another imaging technique, scanning laser opthalmoscopy (SLO), however, this technique is not based on interferometry. The image is formed by collecting all the backscattered light from different depths in the sample and this requires further research.

Theoretical estimation of the defocus Zernike coefficient to correct for a defocus caused by an axial displacement is in excellent agreement with the Zernike coefficient obtained from an optimization maximizing the OCT signal at the given depth. The one step defocus correction can be applied to scanning OCT systems to quickly set the optimal defocus or to easily change the focal point to another depth in the sample. Only well calibrated and well known optical systems allow for this one step defocus correction, in other cases it might be considered as a good first estimate. Note that the defocus is the primary aberration in the human eye [33] and that its corrections leads to the strongest image quality improvement of all aberrations.

The scattering medium OCT signal transfer functions for the single aberrations all exhibit pseudo-convex properties, i.e. they have a global maximum for zero aberrations. A validation for the pseudo-convex properties is given by the convergence results shown in Fig. 8, which show that the algorithm always converged towards the same metric value. The pseudo-convexity shows why hill climbing algorithms such as proposed in [12,14] eventually converge towards a maximum signal. A clearer understanding of how aberrations influence the OCT signal can help in selecting metrics for wavefront sensorless aberration correction, which can lead to faster signal convergence. The OCT transfer functions, as developed here, also allow testing and simulation of new optimization algorithms prior to *in vivo* application.

6. Conclusion

Using Fresnel propagation, overlap integrals and Gaussian distributions two OCT transfer functions modeling the effect of lateral aberrations for a mirror and a scattering medium on the OCT

#226065 - $15.00 USD Received 31 Oct 2014; revised 11 Dec 2014; accepted 11 Dec 2014; published 23 Dec 2014

signal are derived. Measurements on a mirror and a scattering medium with an AO-OCT system closely resemble the proposed transfer functions. A one step defocus correction method has theoretically been derived and successfully applied. The pseudo-convex nature of the transfer function is validated by the 100% convergence success of a hill-climbing algorithm.

Acknowledgments

The authors would like to thank all project partners, and all the technicians involved, especially ing. W.J.M. van Geest and C.J. Slinkman. The authors gratefully acknowledge the funding of the IOP Photonic Devices, project number IPD12020, managed by Rijksdienst voor Ondernemend Nederland (RVO).

#226065 - $15.00 USD Received 31 Oct 2014; revised 11 Dec 2014; accepted 11 Dec 2014; published 23 Dec 2014